Full length article

Interaction and infiltration behavior of Eyjafjallajökull, Sakurajima volcanic ashes and a synthetic CMAS containing FeO with/in EB-PVD ZrO$_2$-65 wt% Y$_2$ O$_3$ coating at high temperature

R. Naraparaju [a, *], Juan T. Gomez Chavez [a, b], U. Schulz [a], C.V. Ramana [b]

[a] German Aerospace Center (DLR), Institute of Materials Research, Cologne, 51170, Germany
[b] Department of Mechanical Engineering, University of Texas at El Paso, El Paso, TX, 79968, USA

A B S T R A C T

Yttria rich-zirconia thermal barrier coatings (TBCs) with a nominal composition of 65 wt % Y$_2$O$_3$ balanced ZrO$_2$ were deposited by electron-beam physical vapor deposition (EB-PVD) and tested for calcium-magnesium-aluminum-silicate (CMAS) infiltration resistance. The infiltration studies were performed with a set of one synthetized CMAS composition and two real volcanic ashes from the Eyjafjallajökull volcano located in Iceland and the Sakurajima volcano located in southern Japan. The coatings were tested at 1250 °C for short term (5 min) and long term (intervals from 1 to 20 h). The results indicate a significantly different reaction process for the synthesized CMAS compared with the natural volcanic ashes. The yttria-rich zirconia coatings demonstrate promising results against infiltration by vigorously reacting against the molten glass inducing its crystallization by forming apatite and garnet phases. The formed reaction products effectively sealed the columnar gaps of the TBC and generated a uniform re-action layer that prevented further infiltration.

© 2017 Acta Materialia Inc. Published by Elsevier Ltd. All rights reserved.

1. Introduction

Thermal barrier coatings (TBCs), which are extensively used in gas turbines and aero-engine parts, protect the metallic surfaces and engine components from high temperature exposure for extended duration. State of the art TBCs used on gas turbine engines provide thermal insulation to the underlying super-alloy components in the hot gas path sections and, thus, allow engines to operate at temperatures as high as 1200 °C, thereby increasing their thermodynamic efficiency [1–3]. The commonly employed state of the art material for TBCs at present is 7–8 wt % Y$_2$O$_3$ stabilized ZrO$_2$ (7YSZ). The 7YSZ TBCs are commonly deposited by air plasma spray (APS) or electron-beam physical vapor deposition (EB-PVD). While 7YSZ TBCs served the industry for many years, currently, significant attention is paid towards the development of novel TBCs which can withstand higher temperatures ($\geq$1300 °C) [4]. Such TBCs with high temperature tolerance can minimize the fuel consumption by maximizing the gas turbine efficiency, which will subsequently help protect the environment through the reduced carbon emissions. Additionally, different fuel compositions ranging from natural gas to broad range of syngas with high hydrogen contents are being tried for next-generation gas turbine power plants [5,6]. Therefore, the TBCs for next-generation gas turbine systems must have the reliability and durability in diverse chemical, thermal and mechanical environments.

The increasing demand for higher operating temperatures in aero-derivative and land-based gas turbines has brought into attention the effects of infiltrated mineral deposits into hot engine's components [7–11]. The siliceous mineral deposits, commonly consisting of calcium-magnesium-aluminum-silicate i.e., CaO-MgO-Al$_2$O$_3$-SiO$_2$ (CMAS), are ingested as sand, runway debris, volcanic ash, air pollution, and fly ash into gas turbines. The CMAS particles deposit on the hot gas path components and melt generating infiltration into the porous TBC structure (regardless of the deposition technique used) resulting in premature failure due to microstructure degradation, sintering and spallation [12]. The molten CMAS infiltrates the columnar gaps, pores and cracks. While flowing inwards into the TBC it hardens as it flows down the thermal gradient. The hardening of the CMAS compound that also occurs during cooling of the whole component generates a stiffening of the TBC which leads to loss in strain tolerance of the

---

coating, thereby generating delamination [13–15]. Subsequently, the interaction of the CMAS melt with the TBC at high temperatures generates a thermo-chemical damage system characterized by the dissolution of the initial metastable tetragonal (t') 7YSZ due to the depletion of Y_2O_3 phase and re-precipitation of Zr with a composition and structure that depends on the CMAS chemistry [14,16].

Due to the serious effects that CMAS attack has on reducing the service life of 7YSZ TBCs, scientific and engineering research community is challenged to better understand the attack mechanisms and design methods for CMAS infiltration resistance. Furthermore, due to the eruption of the Eyjafjallajökull volcano located in Iceland on 2010, the safety regulations for the aviation industry had to be reconsidered due to the large widespread of the volcanic ash cloud generating a substantial economic loss due to the extended air space closure [17,18]. This event motivated the aircraft engine manufacturers to effectively address this volcanic ash (VA) attack issue and reduce economic losses. The most common infiltration mitigation strategies focus on using a reactive material that upon interaction with molten CMAS glass induces its partial or full crystallization sealing the porous features of the coating stopping any further infiltration [7,19–22]. Only a few studies have tested their mitigation strategies with a natural CMAS source such as real volcanic ash or sand [23–25]. Some of the methods proposed include the utilization of overlying coatings on top of the 7YSZ in arresting the CMAS infiltration [26,27]. For instance, Eils et al. [28] have performed studies on a variety of yttria-zirconia coatings (ZrO_2, $Y_2O_3 \cdot ZrO_2$ and Y_2O_3) for CMAS mitigation, where the formation of oxyapatite and garnet phases exhibited promising results against CMAS infiltration. The objective of this work was to study the CMAS infiltration resistance of yttria rich-zirconia with a composition of 65 wt % Y_2O_3 (rest ZrO2) produced by EB-PVD process (65YZ). The ultimate goal is to employ the proposed coating system in multilayer TBC systems based on a standard 7YSZ coating for thermal insulation and a yttria rich-zirconia top coat for corrosion resistance. While high yttria based coatings show a potential for CMAS arrest in TBC systems [19,24,25,28–30], there is no available literature for infiltration tests using real volcanic ash on EB-PVD yttria rich coatings at this time. Thus, a better understanding of the interaction between CMAS/VA with −high yttria coatings at high temperature, as presented and discussed in this paper, can lead to significant benefits in the performance and lifetime extension of TBCs for aero-derivative and land based gas turbine engines.

2. Experimental details

2.1. CMAS and volcanic ash preparation

Two real volcanic ashes (VA) and one synthetized CMAS powder were used for the infiltration studies. The volcanic ashes were collected from site corresponding to the Eyjafjallajökull volcano located in Iceland and the Sakurajuma volcano located in southern Japan. The CMAS powder (CMAS 1) was synthetized matching the chemical composition of CMAS deposits in screened engine hardware, its preparation is described elsewhere [9,31]. The chemical

composition and summary of the used powders are presented in Table 1. Differential scanning calorimetry (DSC) measurements were performed to determine their melting temperatures which are listed in Table 1. The powders were analyzed between room temperature and 1300 °C in a STA 449 F3 Jupiter equipment (Netzsch, Selb, Germany).

2.2. Sample preparation

Yttria-zirconia samples with higher yttria content were coated on alumina (Al_2O_3) substrates using EB-PVD technique. Evaporation was performed using a jumping beam system on dual evaporation sources namely 7YSZ (source 1) and 100 wt % Y_2O_3 (source 2) as seen in Fig. 1. The deposition set up used generated a variation in the yttria content with respect to the location to the evaporation source meaning the closer the sample to the 7YSZ source, the lower the yttria composition. The selected sample composition had a 65 wt % yttria (rest zirconia) and a thickness of 150–165 μm.

2.3. Infiltration experiments

Infiltration experiments were carried out by depositing CMAS/VA on top of the coated TBC samples in the amount of 20 mg/cm². Infiltration temperatures were chosen at 1250 °C for short term (5 min) and long term (1–20 h). Short term tests were performed in a cyclic furnace by heating up the samples to 1250 °C in 8 min, following isothermal heating for 5 min and air quenching to room temperature. Long term tests were performed in a chamber furnace with a heating range of 10 K/min, following isothermal heating for ranges of 1–20 h and furnace cooling to room temperature.

2.4. Characterization

CMAS/VA were mixed with yttria rich zirconia-powder obtained from the as coated samples to determine the formed phases upon CMAS/VA-high yttria reaction. The 65YZ powder was mechanically removed from the as coated samples by scratching it off the substrates. The final powder mixture used for XRD analysis had a composition of 40 wt % CMAS/VA and 60 wt % of yttria rich powder (65 wt % yttria). Subsequently, the powder mixture was heat treated on platinum sheets for 10 h at 1250 °C, followed by furnace cooling to room temperature. The post heat treated powder mixture was mechanically removed from the platinum sheets and crushed using mortar and pestle for30 min to obtain fine powder in order to facilitate the XRD. The measurements were carried out using Si single crystal holders in a Siemens D5000 diffractometer using CuKα radiation with a secondary graphite monochromator (EVA/Topas 4.2 software package, Bruker AXS, Karlsruhe, Germany). Standard metallographic techniques were used for sample preparation in the cross-section analysis. Scanning electron microscopy (SEM) (DSM ultra 55, Carl Zeiss NTS, Wetzlar, Germany) techniques were performed. The system was equipped with an energy-dispersive spectroscopy (EDS) (Inca, Oxford Instruments, Abingdon, UK) to characterize the infiltrated zones and depth of infiltration. The reaction products formed by the interaction of

Table 1
Chemical composition summary for used CMAS/VA.

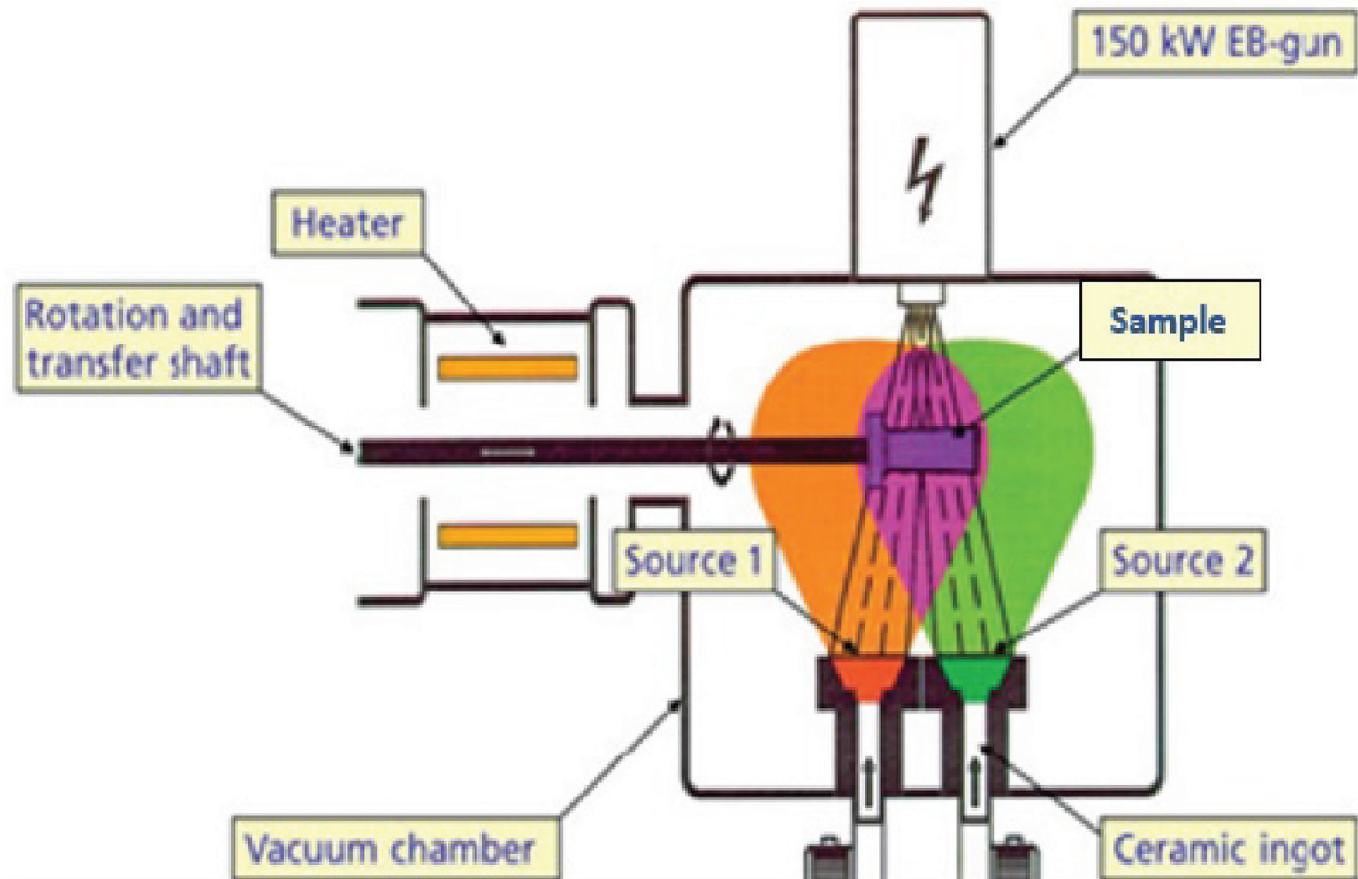| Label	Chemical composition (Mol. %)								Crystalline phase	Melting point
	SiO_2	CaO	MgO	Al_2O_3	FeO	TiO_2	Na_2O	K_2O		
CMAS 1	41.7	24.7	12.4	11.1	8.7	1.6	0.0	0.0	Pryoxene-Anorthite	1250°c
Japan ash	66.3	11.4	0.3	15.7	1.4	0.0	4.3	0.7	Anorthite-Amorphous	1170°c
Iceland ash	49.7	12.5	6.1	7.4	17.6	4.3	2.0	0.4	Amorphous	1150°c

Fig. 1. Two source evaporation process schematic.

CMAS/VA with TBC were characterized by matching composition obtained from XRD results and chemical composition from EDS spot analysis. Infiltration depth was confirmed by tracing Si amounts using EDS elemental mapping and spot analysis. Transmission electron microscopy (TEM) analysis was performed on cross sectional samples selected from reacted interfaces via focused ion beam sectioning (FIB) in a FEI Helios Nanolab 600i FIB system and a Tecnai F30 (STEM) using a field-emission gun (FEI Inc., Eindhoven, Netherlands).

3. Results

3.1. As coated 65YZ characterization

The high yttria −zirconia TBC deposited by EB-PVD in conventional rotation mode grew in a columnar microstructure as seen in Fig. 2a. The columns have a lower density than standard 7YSZ TBCs. Additionally, the 65 YZ columns show in some areas more column branching compared to 7YSZ, i.e. within one column smaller subcolumns that grow slightly of-axis form. Under the deposition conditions used, namely the two source evaporation and an average substrate temperature of 900 °C most columns do not grow very parallel and very well ordered as it can be achieved for 7YSZ. As a consequence the width and shape of the inter-columnar gaps varies to some extend within the samples locally. It is important to highlight that process parameters have not been optimized yet to tailor the coating morphology. The feather arms features located at the edges of the TBC columns (Fig. 2b) are somewhat similar in distribution and dimensions to the ones commonly obtained in standard 7YSZ. .

3.2. Melting behavior of CMAS and VA

The results obtained from the DSC measurements of CMAS and VA are presented in Fig. 3. The studies were performed to determine the melting points of the CMAS/VA sources. The results for all the powders are plotted for the range of 500–1300 °C. The CMAS 1 composition (Fig. 3a) shows a clear endothermic peak in the range of 1225–1260 °C which represents the melting process. The powder starts to melt at 1225 °C and progresses to a fully molten stage at about 1250 °C. The VAs exhibit a non-linear DSC profile as seen in Fig. 3b and c.The Japan VA exhibits a large depression which is formed after 1100 °C, it appears to be the endothermic peak representing the partial melting point. The depression reaches a low point at about 1175 °C which is considered as the temperature at which the glass is fully molten. The Iceland VA exhibits a significant endothermic peak from 1060 °C to 1150 °C referring to the broadest melting range for the CMAS/VA powders. The crystalline nature of CMAS 1 generates the narrowest melting range (1225–1250 °C) and the highest melting point at which the material is in fully molten state (1250 °C). The summary of the melting point and crystalline phases present in the powders are as listed in Table 1.

3.3. Characterization of CMAS/VA-yttria rich TBC mixtures

The XRD patterns obtained for the powder mixtures of CMAS/VA-yttria rich zirconia at 1250 °C for 10 h are shown in Fig. 4. Three main phases were identified for all three CMAS/VA
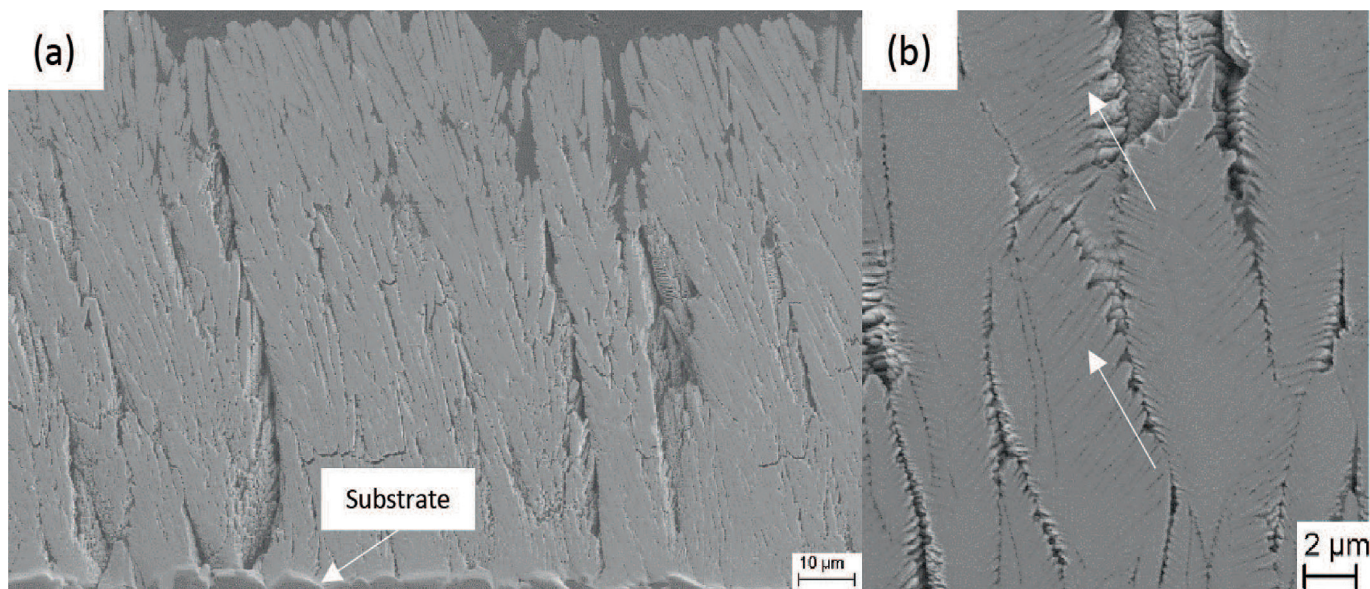
Fig. 2. (a) Cross section view of the EB-PVD 65 wt% yttria-zirconia TBC in the –as coated stage/condition. (b) High magnification view showing feather arms features (white arrows).
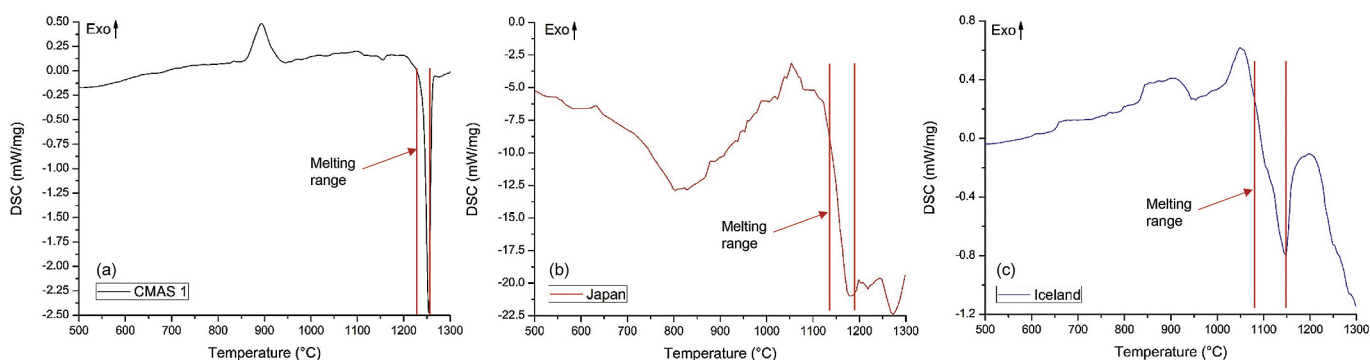

Fig. 3. DSC plots for (a) CMAS 1, (b) Japan VA, (c) Iceland VA. Melting range delimited in red bars exhibits the range at which the CMAS/VA transitions from partially molten to fully molten state. (For interpretation of the references to colour in this figure legend, the reader is referred to the web version of this article.)
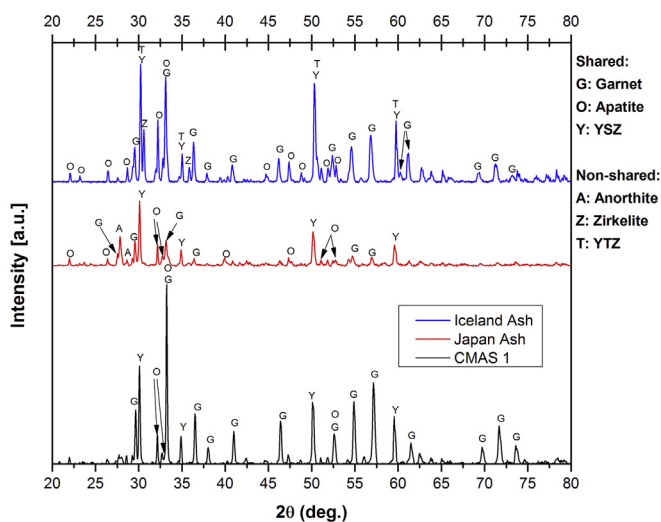

Fig. 4. XRD results for the powder mixtures at 1250 °C for 10 h using CMAS/VA mixed with 65 wt % yttria rich-zirconia powder.

compositions: garnet, apatite and YSZ. The phases are labeled throughout the whole paper (starting in Fig. 4) as G, O and Y respectively. The first shared phase identified as garnet (G) exhibits the highest intensity for CMAS 1, followed by Iceland VA and Japan VA. For all the used powders, the garnet phase exhibited a peak overlap for two garnet types identified as Aluminum Iron Yttrium Oxide ($Al_4FeY_3O_{12}$) and Andradite ($Ca_3Fe_2(Si_3O_{12})$). A better peak match and intensity was shown for the $Al_4FeY_3O_{12}$ garnet in the VA mixtures. In the case of CMAS 1, the garnet providing better match was andradite. The second common phase in the powder mixtures also exhibits a peak match overlap for Calcium Yttrium Oxide Silicate ($Ca_2Y_8(SiO_4)_6O_2$) and $Y_{9.33}(SiO_4)_6O_2$. The last identified phase, which is common in all the powder compositions, corresponds to a cubic phase identified as Zirconium Yttrium Oxide or YSZ (Y) ($Zr_{0.82}Y_{0.18})O_2$. This phase only exhibits a peak overlap with the Iceland VA-yttria rich zirconia mixture with the phase identified as Yttrium Titanium Zirconium Oxide or YTZ (T) ($Zr_{0.62}Y_{0.20}Ti_{0.18}O_{1.90}$). Additionally, one extra phase was identified only for Iceland VA exhibiting a mid- and low-intensity peaks at about 31 and 36° respectively. The mentioned phase was identified as Zirkelite (Z) ($CaZrTi_2O_7$). Finally, the Japan ash mixture exhibited one mid-intensity peak at about 27.5° corresponding to the common

silicate mineral anorthite ($CaAl_2Si_2O_8$) which carries the common CMAS elements corresponding to the unreacted crystallized ash.

3.4. Short term infiltration

The short term infiltration tests for 5 min at 1250 °C were performed to categorize the initial reaction products formed upon molten glass/TBC interaction. These studies revealed which products contribute to the initial glass crystallization and reactivity. Fig. 5 shows the cross section SEM image of the infiltrated coatings after 5 min. The data shows that the infiltration of the unreacted glass is not uniform by showing deeper glass infiltration where large inter-columnar gaps are available due to the non-uniform morphology generation described above. The estimation of the infiltration depth is generated by measuring an overall infiltration area (delimited in dotted bars in Fig. 5a, b and c) where no big gaps were available for deep glass infiltration. The infiltration depth is estimated as 38, 28 and 28 μm for CMAS 1, Japan and Iceland VA respectively. Fig. 5d, e and f represent the high magnification images of the reaction zone generated at the glass/TBC interface delimited in the single rectangles from Fig. 5a, b and c. The image shows the reaction product formation upon interaction of glass/ TBC. It also shows how yttria reacts vigorously with CMAS/VA after

short time by generating reaction products that induce glass crystallization which seals the open gaps available for infiltration. The reaction products appear to conglomerate at the TBC/molten glass interphase and up to about 10 μm under for all cases (Fig. 5d, e and f).

These reaction products formed were identified by comparing the composition obtained from EDS spot analysis and the results obtained from the XRD powder mixtures. Fig. 6 shows the initial reaction within an inter-columnar gap which is inducing crystallization of the glass. For the CMAS 1 case shown in Fig. 6a, the main product generated upon crystallization appears to be garnet (G) which exhibits all available cations (Si, Ca, Al, Mg, Fe, Y, Ti) with a singular Fe-Y enrichment compared with apatite product. It is seen as a light gray product growing at the edge of the TBC columns and progressively covering the unreacted glass (g) seen as dark gray. Additionally, small localized traces of the apatite phase (O) were found and identified as small flake shaped particles with a lighter gray coloration. The last product identified in the reaction was the zirconia rich YSZ product (Y) which was seen in all the compositions as a white bright particle. The chemical composition summary for the found reaction products is provided in Table 2a for CMAS 1.

The reaction products for the Japan VA case are shown in Fig. 6b where a different reaction nature is seen compared with CMAS 1.
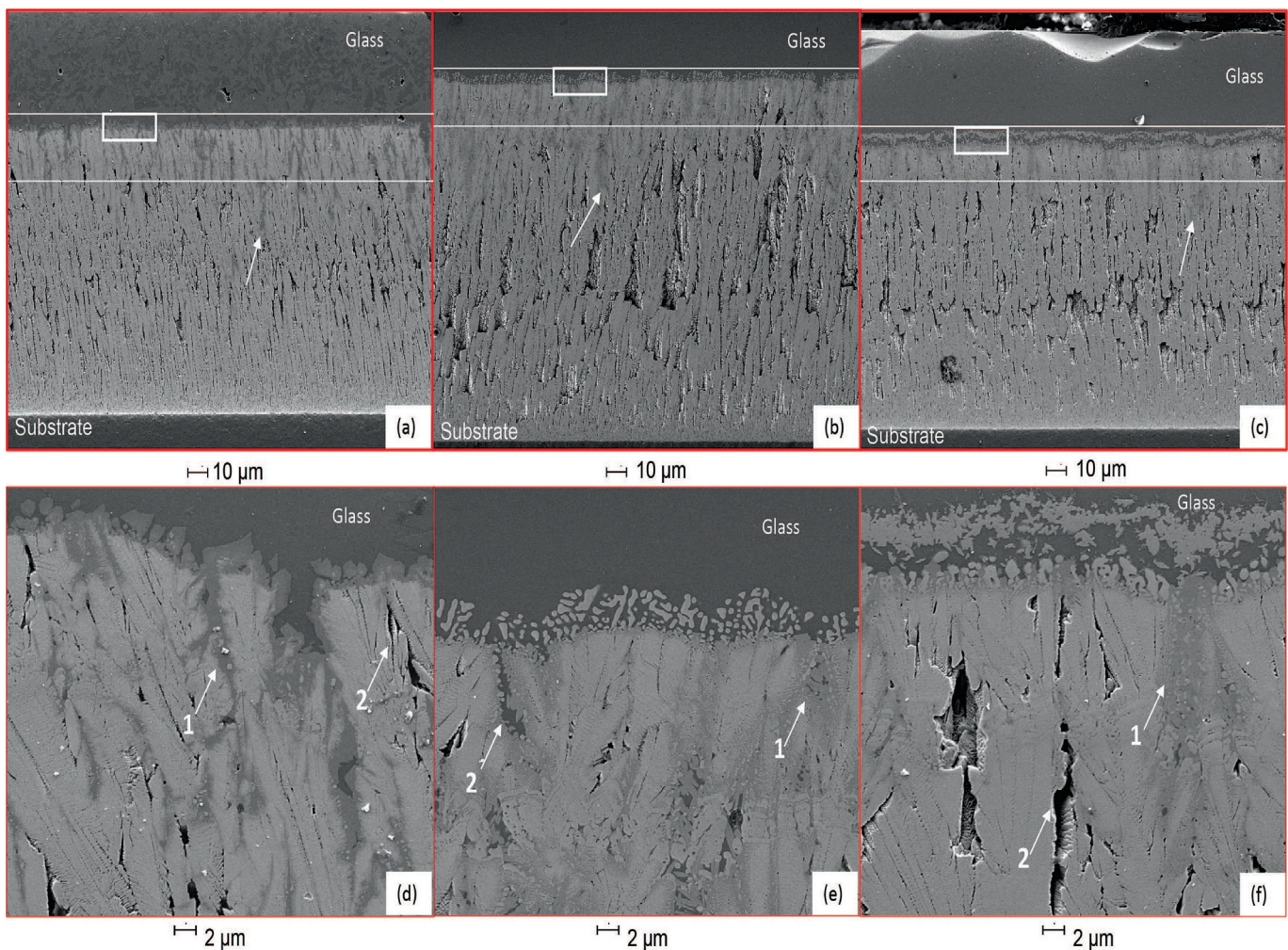
Fig. 5. Cross section SEM view for the infiltrated coatings after 5 min infiltration test at 1250 °C for (a) CMAS 1, (b) Japan VA and Iceland VA. The area delimited in dotted bars represents the overall infiltration zone used for infiltration estimation. Single arrows represent the large inter-columnar gaps where deep glass infiltration was found. The area delimited in the single rectangles represents the high magnification image of the reaction zone at the glass/TBC interface for (d) CMAS 1, (e) Japan VA and (f) Iceland VA. The areas labeled as 1 show the columnar gaps being sealed by the formation of reaction products. Areas labeled as 2 show the open columnar gaps susceptible for glass infiltration.
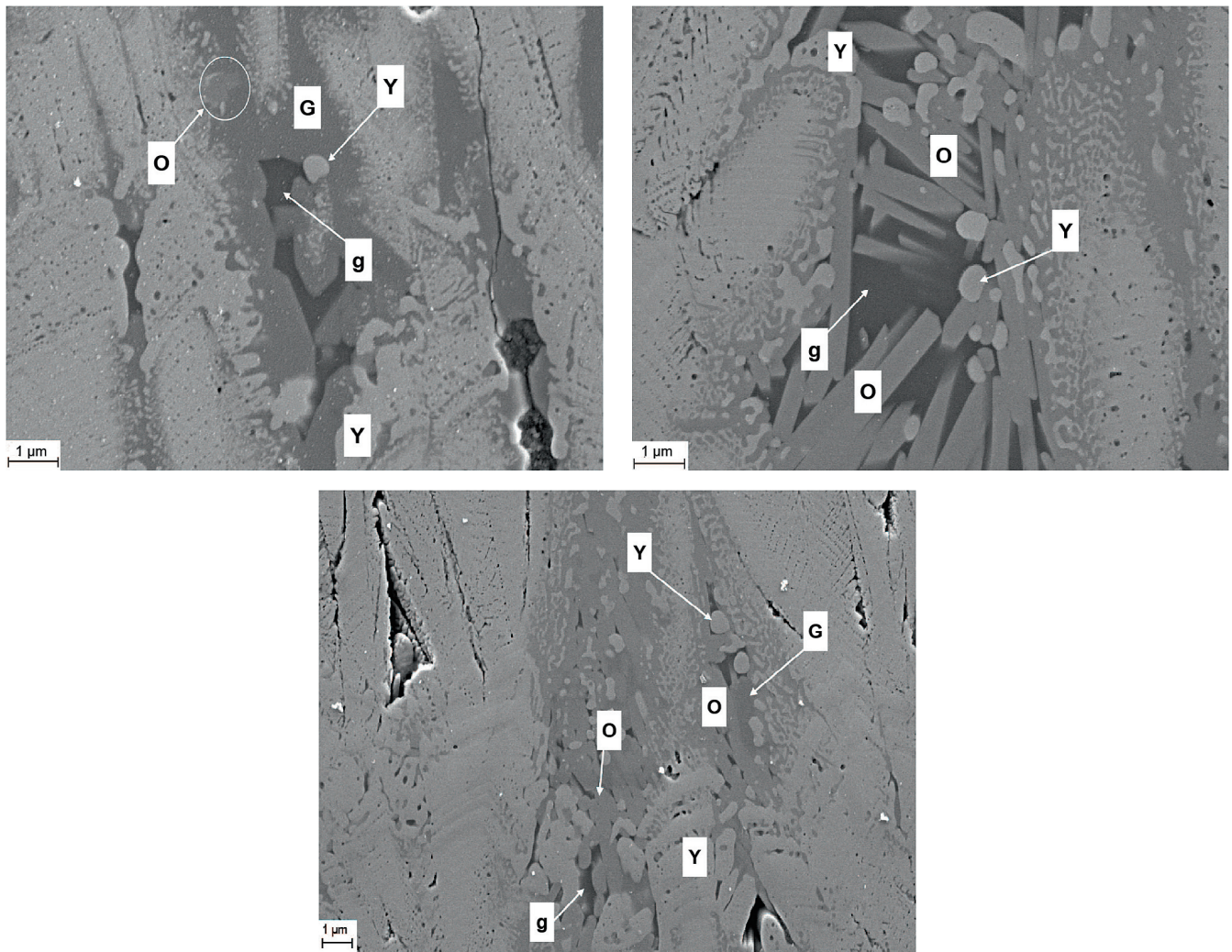
Fig. 6. a: Columnar gap sealing process for CMAS 1 at 1250 °C for 5 min. b: Columnar gap sealing process for Japan VA at 1250 °C for 5 min. c: Columnar gap sealing process for Iceland VA at 1250 °C for 5 min.

Table 2a
Normalized composition for the reaction products for CMAS 1 at 1250 °C.

Time	Label	Chemical composition (mol %)								Phase
		Si	Ca	Ti	Mg	Al	Fe	Y	Zr	
5 min	G	26.5	18.8	2.0	9.5	12.7	16.9	13.6	0.0	Garnet
20 h	G	25.3	17.6	1.5	9.8	14.1	15.8	15.8	0.0	Garnet
5 min	A	40.6	20.3	0.0	1.6	35.2	2.4	0.0	0.0	Anorthite
20 h	A	41.8	20.0	0.0	2.2	33.4	2.7	0.0	0.0	Anorthite
5 min	Y	3.3	2.4	0.0	1.4	2.1	1.9	24.0	64.9	YSZ
20 h	Y	0.0	0.0	0.0	0.0	0.0	0.0	21.8	78.2	YSZ

Table 2b
Normalized composition for the reaction products for Japan VA at 1250 °C.

Time	Label	Chemical composition (mol %)								Phase
		Si	Ca	Ti	Mg	Al	Fe	Y	Zr	
5 min	O	38.5	9.4	0.0	3.5	2.9	0.0	45.7	0.0	Apatite
20 h	O	38.3	10.2	0.0	1.7	2.1	0.0	47.7	0.0	Apatite
5 min	Y	16.7	3.1	0.0	2.4	4.6	2.8	25.8	44.6	YSZ
20 h	Y	0.0	0.0	1.2	2.6	5.0	2.0	22.0	67.2	YSZ
1 h	C	46.5	2.0	0.0	1.2	1.6	0.9	41.5	6.2	Yttrium silicate
20 h	C	48.6	1.3	0.0	0.0	0.0	0.0	45.3	4.8	Yttrium silicate

The reaction formed for Japan VA exhibits the formation of large faceted crystals reacting against the molten VA glass (g). The large faceted crystals matched the apatite (O) composition by mostly showing amounts of Y, Si, Ca and very small traces of Mg and Al as seen in Table 2b. The reaction zone does not exhibit traces of Fe rich garnet (G) which indicates that the only phase that forms rapidly and act against glass infiltration appears to be apatite. The YSZ phase (Y) is also found in this composition with a bright white globular shape particle.

Finally, the reaction products for Iceland VA exhibit a similar arrangement compared with Japan VA as seen in Fig. 6c. The main crystallization products also appear as faceted type crystals with a smaller size and more prismatic shape. The mentioned crystals matched the composition for the apatite phase (O). A conglomerated particle is exhibited in this reaction with a darker gray coloration compared with the apatite appearance. The product is identified as garnet (G) with all available cations in its composition as seen in Table 2c and also exhibiting the particular Fe-Y enrichment. Finally, the YSZ phase is also identified in the reaction zone (Y) with the same characteristics exhibited for Japan VA.

Table 2c
Normalized composition for the reaction products for Iceland VA at 1250 °C.

| Time	Label	Chemical composition (mol %)								Phase
		Si	Ca	Ti	Mg	Al	Fe	Y	Zr	
5 min	G	18.8	6.3	0.0	9.9	16.1	16.1	28.4	2.8	Garnet
20 h	G	19.6	8.7	0.9	9.4	10.3	25.7	25.4	0.0	Garnet
5 min	O	30.0	8.5	0.0	3.8	7.4	3.3	40.8	4.0	Apatite
20 h	O	44.2	9.6	0.0	2.1	6.1	1.3	36.6	0.0	Apatite
5 min	Y	5.0	2.5	4.9	2.1	1.7	4.2	28.1	51.7	YSZ
20 h	Y	0.0	0.0	3.5	0.0	0.0	4.5	24.9	67.1	YSZ
5 min	d	38.6	5.4	2.8	7.2	11.8	24.2	7.1	2.8	Garnet dendrite
20 h	d	38.7	9.1	1.3	9.4	12.6	16.2	12.7	0.0	Garnet dendrite
5 min	T	5.9	2.5	19.4	1.6	4.0	17.8	21.8	26.9	YTFZ
20 h	T	5.8	1.5	20.2	1.1	5.0	19.4	20.6	26.4	YTFZ

3.5. Long term infiltration

The long term infiltration tests were performed to study the coating infiltration resistance and the stability of reaction products after thermal tests in intervals of 1, 5, 10 and 20 h (4 tests per composition). The glass infiltration followed the same behavior shown for the short term where deep infiltration is exhibited in microstructural zones where large inter-columnar gaps were available. Fig. 7 shows the cross sectional SEM image for Iceland VA after 20 h infiltration at 1250 °C with its respective Si elemental mapping for infiltration depth screening. The image clearly shows a deeper infiltration exhibited at the presence of large columnar gaps (single arrows) compared to the overall infiltration zone delimited within the white bars where lower glass infiltration is exhibited due to the more densified microstructure and sealing of the smaller gaps by the crystalline reaction products. Fig. 8 shows the infiltration depth progression measured at the overall infiltration zone for the 3 compositions tested at 1250 °C from 5 min to 20 h. The deepest infiltration was exhibited by CMAS 1 (65 μm), followed by Iceland VA (60 μm) and Japan VA after 20 h (45 μm). The infiltration depth plot shows a nearly linear trend in the infiltration after 10 h of thermal exposure for all the used compositions, i.e. the thickness
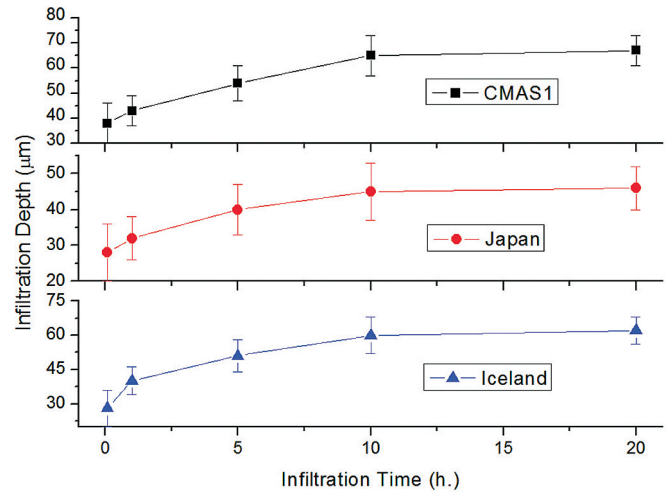

Fig. 8. Infiltration depth plot for used CMAS/VA compositions at 1250 °C from 5 min to 20 h. The measurement is performed at the overall infiltration zone shown in Fig. 6.

of the overall infiltrated zone does not further grow in thickness significantly.

The reaction layer on top of the TBC columns can be defined as the main reaction zone where all new reaction products coexist together forming a uniform layer which is formed at the molten glass/TBC interface. This reaction layer is formed for all 3 used compositions. The total reaction layer for CMAS 1 is considered from the formation of the garnet phase to the end of the YSZ phase (G and Y respectively). The reaction layer was studied for all the compositions to characterize its growth with respect to time and to identify the stability of the generated products. The elemental mapping of the reaction layer formed for CMAS 1 after 1 h infiltration is shown in Fig. 9a, where it can be confirmed that the main reaction product forming at the interface with a cloud shape is garnet (G) with a clear concentration of Fe (as seen from elemental
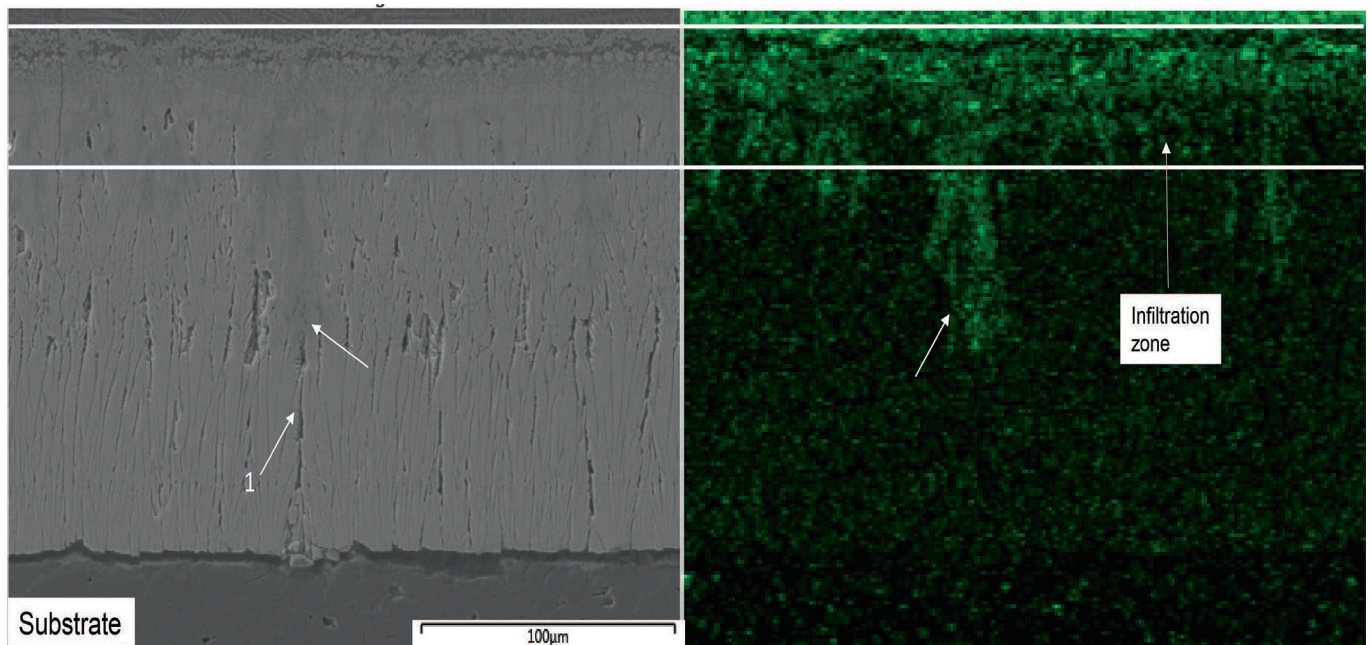
Fig. 7. Cross-section view for infiltrated Iceland VA sample at 1250 °C for 20 h. Right side image shows the corresponding Si elemental mapping. Single arrows indicate the deep infiltration localized at large inter-columnar gaps. Area marked as 1 shows the large columnar gap susceptible for glass infiltration.
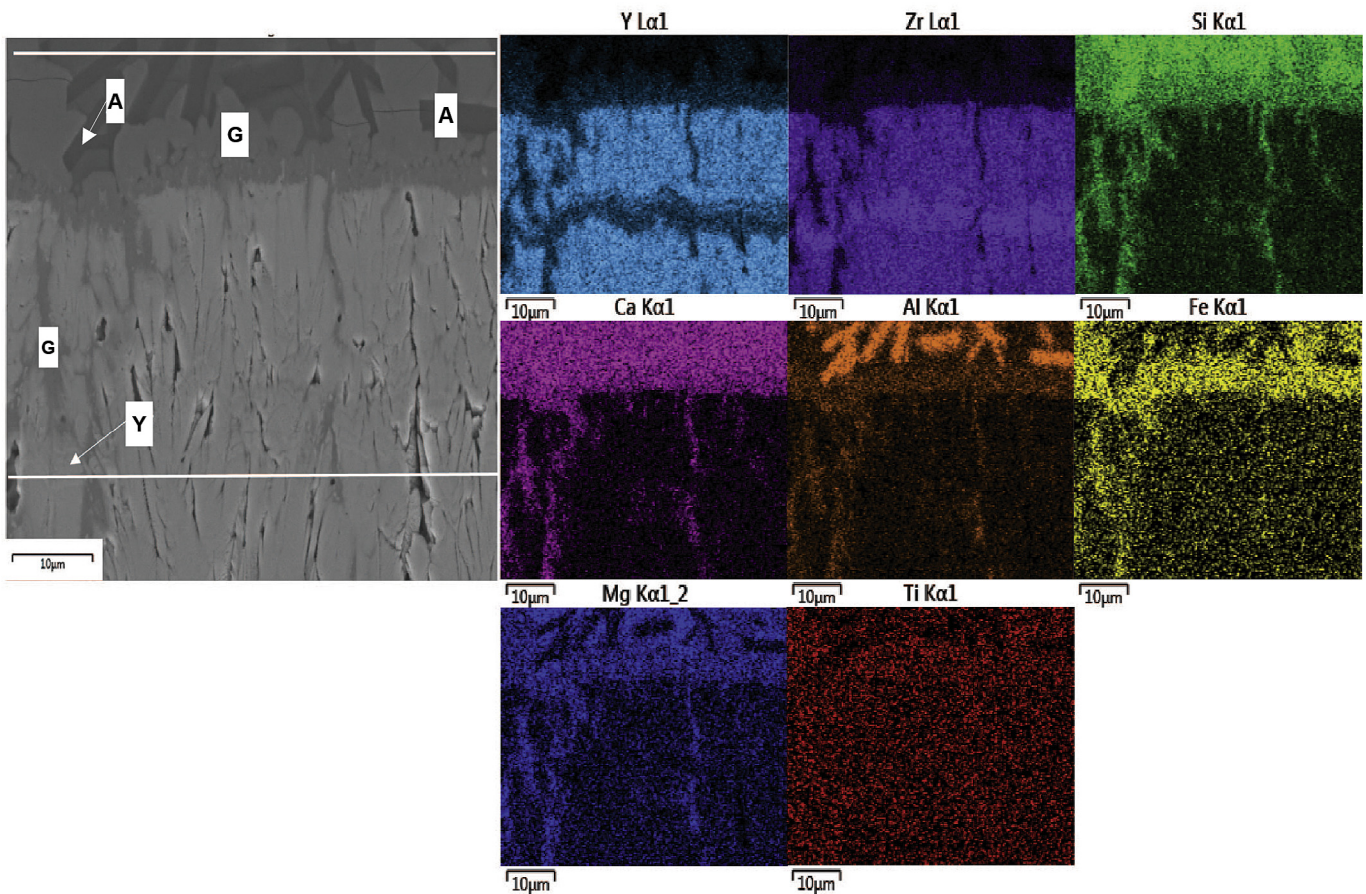
Fig. 9. a: SEM cross section of the reaction zone delimited by white bars at glass/TBC interface for CMAS 1 at 1250 °C for 1 h and corresponding reaction elements mappings. b: SEM cross section of the reaction zone delimited by white bars at glass/TBC interface for Japan VA at 1250 °C for 1 h and corresponding reaction elements mappings. c: SEM cross section of the reaction zone delimited by white bars at glass/TBC interface for Iceland VA at 1250 °C for 1 h and corresponding reaction elements mappings.

mapping). A new reaction product is formed on top of the garnet with a dark coloration and prismatic shape with a clear concentration of Al, Ca and Si. The product is identified as anorthite (A) and it does not exhibit sealing characteristics for the columnar gaps as exhibited by the garnet phase since it only accumulates on top of the reaction layer in localized regions. The elemental mapping confirmed the formation of the YSZ phase which clearly exhibited a Zr enrichment with low amounts of Y as seen in the band located at about 15 μm under the TBC surface (Fig. 9a). The spot analysis also confirms the Zr enrichment in the phase with a Y:Zr ratio of 1:3.58 at %. The phase clearly shows a Y depletion when compared to the Y:Zr ratio from the original coating composition (1:0.84 at %). A similar trend in the Y depletion for the YSZ phase was also found for the VA samples (1:3 for Japan and 1:2.7 for Iceland) confirming the reactivity of yttria with CMAS/VA inducing the formation of new crystal phases that improve the infiltration resistance of the coating. The apatite phase (O) was only traced in small localized areas such as small cracks or in the feather arms where small amounts of molten glass were available to initialize the reaction. After 1 h of isothermal heating, the reaction layer exhibits a uniform thickness of 22 μm which progresses up to 35 μm after 20 h. The garnet and YSZ layers showed a uniform thickness as well of 12 and 3.8 μm respectively. Fig. 10a shows the progression of the reaction layer for the infiltration tests performed at 1250 °C for CMAS 1. The image shows the appearance of the reaction layer and its progression with respect to time. There are no significant changes in the reaction layer regarding the formation of crystalline phases

which remain the same after 20 h of thermal exposure. The garnet phase (G) is still present as the main glass crystallization product after 20 h of heat treatment. Moreover, the garnet exhibits a constant growth in thickness with respect to time with an initial thickness of 4 μm after 5 min ending with 21 μm after 20 h of thermal exposure.

The case for Japan VA, the reaction layer exhibits a large portion of enlarged faceted crystals with a thickness up to 17 μm after 1 h of heat treatment as shown in Fig. 9b. The elemental mapping and spot analysis on those crystals show enrichment in Si and Y with low traces of Ca. The mentioned products (C and O) appear to be the main reaction products exhibiting glass crystallization and columnar sealing properties. The garnet phase (G) was found in small localized areas with Fe enrichment and no traces are found after long term heat treatment (20 h) however, its presence is neglected as a glass arrest product due to the low traces found. The YSZ phase (Y) was found at the end of the reaction zone as typically seen for all the CMAS/VA compositions with a Zr enrichment and Y depletion as seen by elemental mapping shown in Fig. 9b. Additionally, small globular particles matching the YSZ phase composition were found at the top of the reaction layer as well. After 20 h, a significant growth in the "C" crystals is exhibited followed by a reduction in the YSZ particles as shown in Fig. 10b. The constant growth of the faceted (C) crystals appears to be due to the constant Y diffusion from the TBC which promotes the precipitation of the large faceted particles (C) which are first formed after 1 h with a thickness of 10 μm which progresses with time reaching a thickness

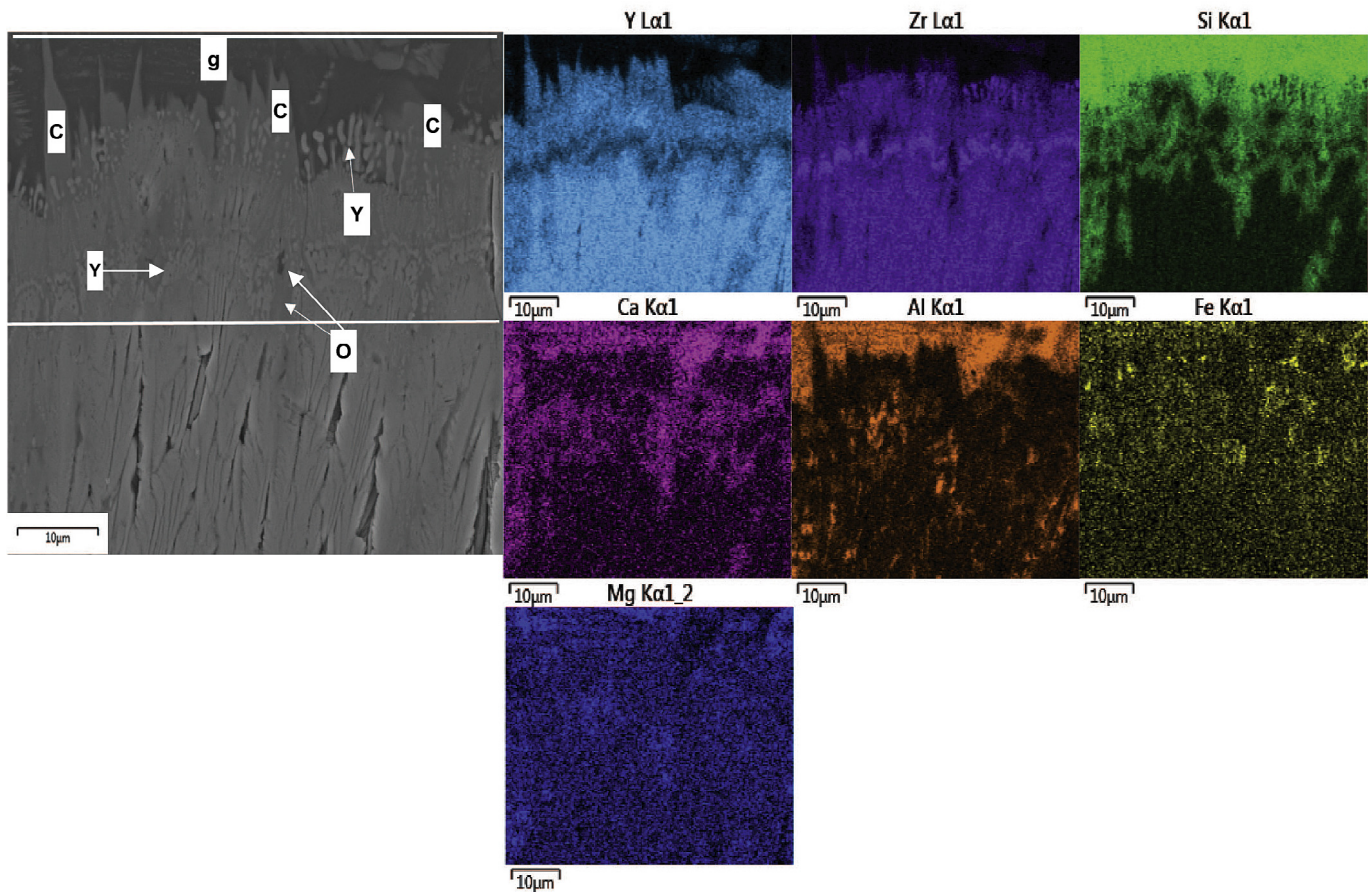**Fig. 9.** (continued).

up to 24 μm after 20 h. TEM analysis shown in Fig. 10e confirms this phase as yttrium silicate. (C). Additionally, apatite (O) products were also identified in the reaction zone as small faceted particles and the apatite phase was confirmed by TEM results shown in Fig. 10d.

The reaction layer formed for Iceland VA at the glass/TBC interface is shown in Fig. 9c for 1 h infiltration test. A uniform layer is formed with enlarged globular and decomposed TBC columns in combination with a uniform layer of dark gray conglomerated particles. The mentioned layer was identified as garnet phase (G) since it exhibited enrichment in Fe and Y with amounts of Si, Al, Ca, Ti and Mg by EDS mapping. The apatite (O) phase was present in the reaction layer in combination with garnet. The apatite phase was present as small prismatic particles with a light gray coloration present in areas with low Fe concentration especially columnar gaps. The YSZ phase was confirmed as well exhibiting its common Zr enrichment and Y depletion at the bottom of the reaction layer. Two additional phases were found in the reaction layer located at the top of the interface. The first phase located in the glass zone on top as small dendritic particles embedded in unreacted glass exhibited a chemical composition matching the garnet phase. The described particles exhibited the distinguished Fe-Y enrichment with concentrations of all available CMAS elements (Ca, Mg, Al, Si and Ti). However, the phase identified as garnet dendrite (d) was only found at the top of the reaction layer in the glass zone with no direct interaction with the TBC. The last found phase was located at the top of the reaction zone as white particles with combination of rounded and prismatic particles. The elemental mapping and spot analysis reveals that the phase is made of Zr, Y, Fe and Ti. From its

chemical composition, the phase could be identified as YTFZ (T). Fig. 10c shows the progression in the reaction layer with respect to time. The image shows a recession of the conglomerated garnet phase (G) after 5 h of isothermal heating. The recession is followed by the formation of small prismatic crystals coexisting with the YSZ globular particles. After 20 h the recession is more noticeable with a significant reduction in the garnet phase and larger appearance of apatite prismatic crystals (O). Additionally, a reduction in the YSZ phase is also seen after 20 h followed by an increase in the amount of embedded garnet dendrite particles (d). The increase in these particles suggests that after longer time, considerable amounts of Y are carried out due to diffusion with the Fe rich glass promoting the formation of the dendritic particles of garnet nature. The top dendritic garnets appear to be a sub-product from the long term exposure due to Y diffusion process since they are hardly traceable after 5 min infiltration.

4. Discussion

4.1. 65YZ TBC composition

The used 65YZ composition gives a 67 Mol% $YO_{1.5}$ which according to yttria -zirconia phase diagram [32,33], and at the deposition parameters of about 900 °C the expected phase should be within the range of $Zr_3Y_4O_{12}$ + Cubic Y_2O_{3ss}. However, according to literature the predicted phase from the phase diagram is hard to be stabilized. In this case the composition identified from XRD analysis is confirmed to be a cubic yttria-zirconia fluorite phase solid solution.
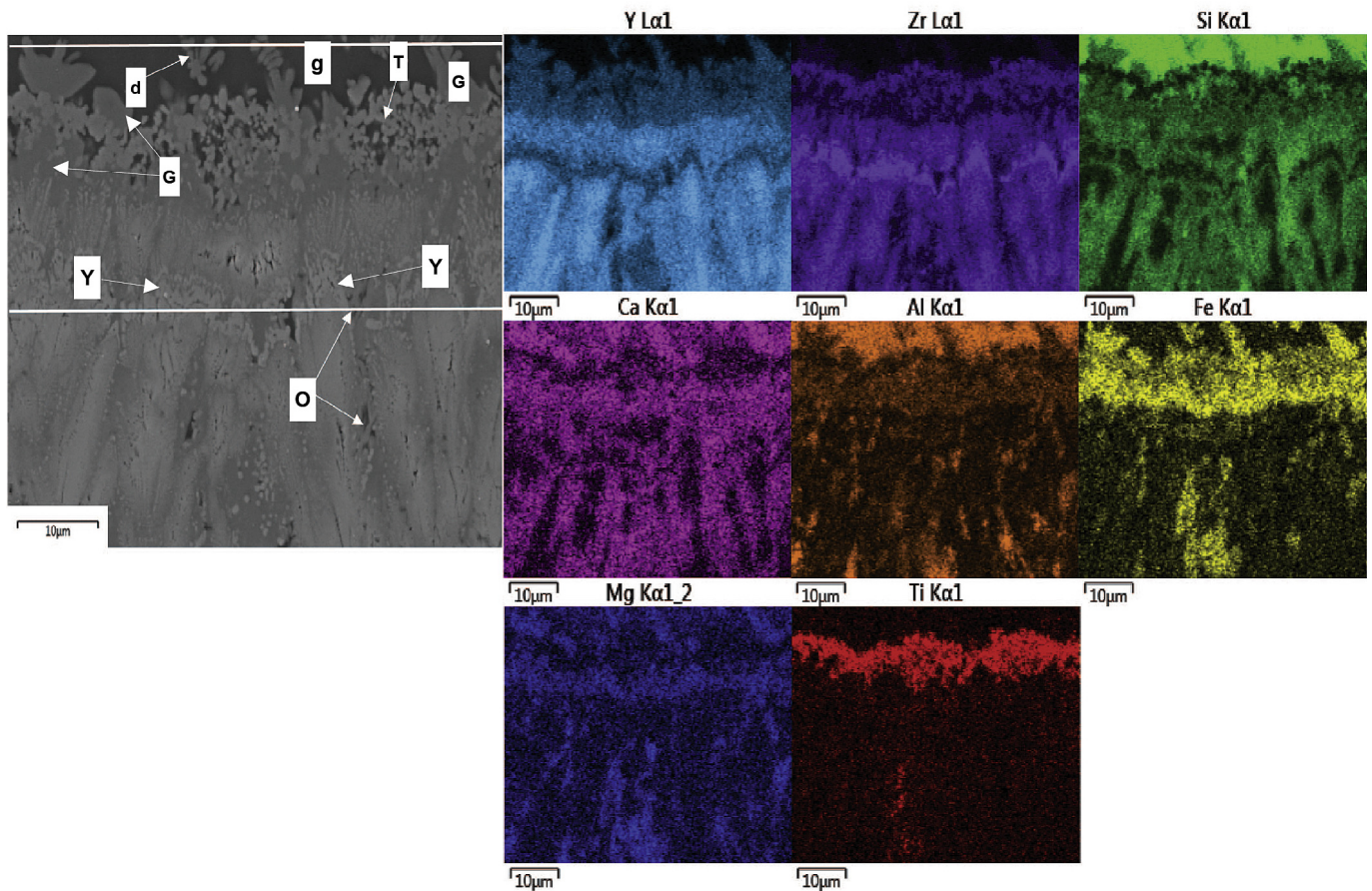
Fig. 9. (continued).

4.2. Infiltration depth analysis

The infiltration depth progression is shown in Fig. 8 for the CMAS/VA compositions at the overall infiltration zone for all the performed experiments at 1250 °C ranging from 5 min to 20 h. The infiltration exhibits stabilization for all compositions by showing a nearly linear behavior in the infiltration curve after 10 h of heat treatment which is confirmed after 50 h of infiltration test (not published) by showing a similar infiltration depth ranging in ±5 μm for all compositions. This suggests that the reaction products remain as stable crystalized products after long term heat treatment avoiding further glass infiltration. The infiltration depth depends on a variety of aspects such as: (i) Morphology of the coating, which defines shape and size of the inter-columnar gaps as well as micro-features of the columnar structure such as geometry of the feather arms at the column edges. It is believed that feather arms influence the infiltration kinetics by changing the tortuosity of the infiltration channels, and they provide a high surface area for rapid phase reactions [34]. (ii) Viscosity of the infiltrating molten or semi-molten deposit. (iii) The reaction kinetics between the melt and the TBC. In the current paper morphology was kept constant, so mainly the influence of the competing process infiltration of the molten glass and phase formation could be studied. Both processes show a temperature dependent kinetic which complicates the situation in real engines. In the 5 min infiltration case the infiltration kinetics is governed by the capillary forces only since the glass crystallization is barely starting at that point. At this point the maximum infiltration is exhibited by CMAS 1 with an infiltration depth of 35 μm. Results obtained from viscosity calculations by considering the

chemical composition of the molten fluids using the model proposed by Giordano et al. [35] predicted the lowest viscosity at for CMAS 1 followed by Iceland VA and Japan VA as seen in Fig. 11. The infiltration results are in agreement with the viscosity calculations at 1250 °C by showing the highest infiltration depth for the less viscous fluid which is CMAS 1 and followed by Iceland VA. Japan VA exhibited the lowest infiltration depth as expected from the viscosity calculations at 1250 °C since it exhibited the highest predicted viscosity. Previous experiments performed on standard 7YSZ coatings at 1250 °C heat treatment for 10 h with the used CMAS 1 composition showed a poor infiltration resistance for standard 7YSZ. The results show a full infiltration after 10 h for 425 μm thick TBCs. Only at a lower temperature of 1225 °C a reduction in infiltration depth could be achieved by tailoring the microstructure of the columns to a more feathery morphology [34]. Yttria rich coatings exhibit a much better infiltration resistance compared to standard 7YSZ due to the formation of stable Y-based crystalline products generated upon interaction of molten glass with the TBC. The reaction products that appear to be formed from glass crystallization are garnet (G) and apatite (O) which block the open TBC gaps, thereby preventing further infiltration. Eils et al. reported the formation of a garnet phase exhibiting CMAS sealing properties using yttria rich-zirconia coatings, the garnet was characterized with a peak match for the composition named "YAG" ($Y_3Al_5O_{12}$) [28]. Additionally, the apatite phase (O) has been reported in literature for yttria rich CMAS resistant coatings as the main CMAS glass arresting product [19,25,28–30] and for $Gd_2Zr_2O_7$ based coatings as well [22,23]. The deep infiltration exhibited in large inter-columnar gaps is believed to occur during the initial melting
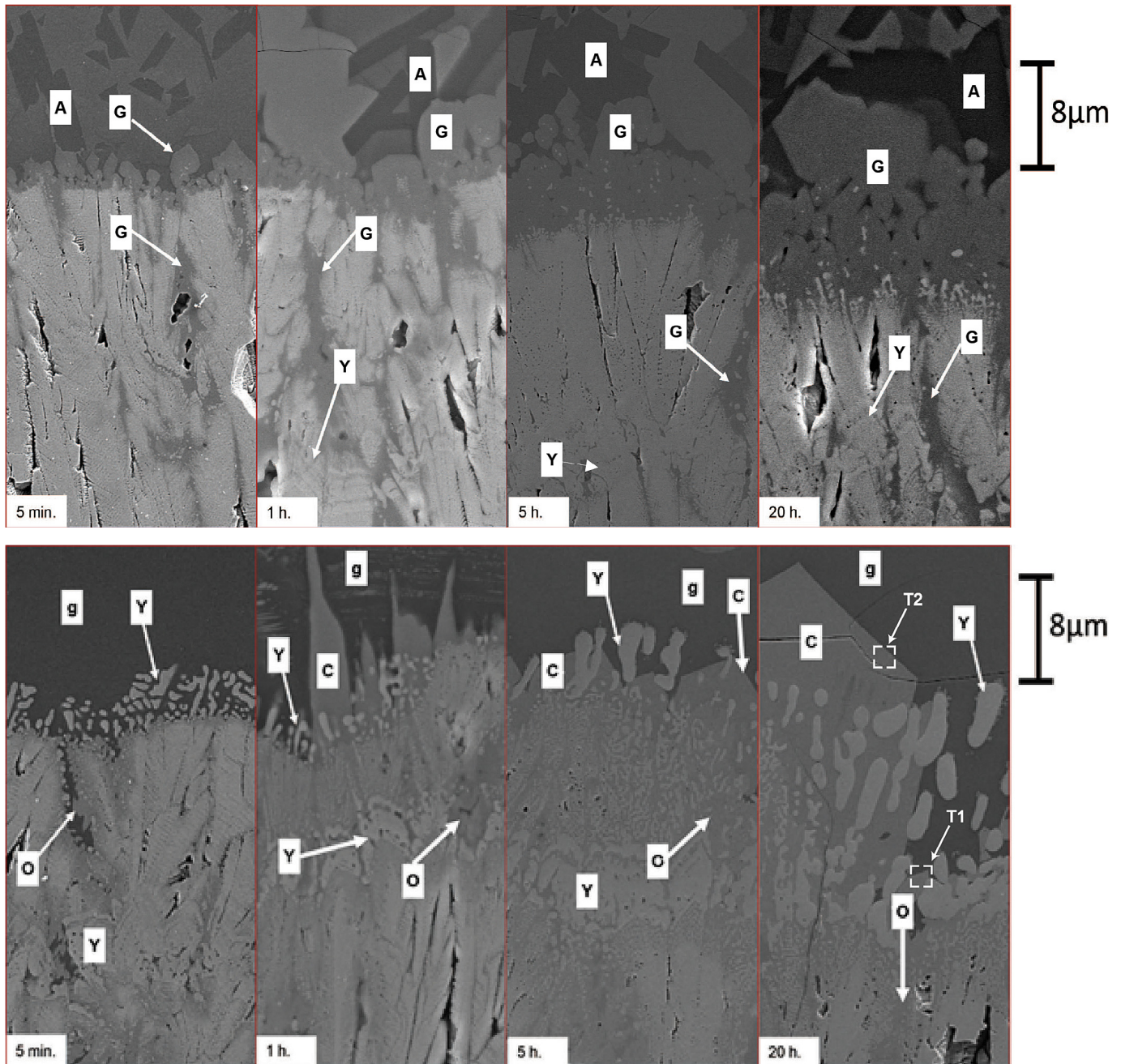
Fig. 10. a: Reaction layer progression with respect to time for CMAS 1 at 1250 °C. b: Reaction layer progression with respect to time for Japan VA at 1250 °C. c: Reaction layer progression with respect to time for Iceland VA at 1250 °C. d: TEM bright field image for the apatite particle (O) obtained from the area marked as T1 in Fig. 10b. The results show the hexagonal apatite structure with the following lattice parameters: a = 9.5 Å, b = 9.5 Å, c = 6.9 Å. e: TEM bright field image for the yttrium silicate particle (C) obtained from the area marked as T2 in Fig. 10b. The results show the monoclinic $Y_2Si_2O_7$ structure with the following lattice parameters: a: 6.87 Å, b: 8.96 Å, c: 4.71 Å.

process since similar infiltration depth up to 120 μm was found at large columnar gaps for all infiltration tests performed (5 min–20 h). The presence of large inter-columnar gaps in the coating microstructure are due to the evaporation technique used where the jumping beam does not allow a uniform evaporation thus, a low densified microstructure was achieved with large inter-columnar gaps open for deep infiltration. This microstructural issue can be most likely eliminated by the use of a single evaporation source and more optimized evaporation parameters such as lower chamber pressure and higher deposition temperature as described by Schulz et al. [36], which is the topic of future research. The two-

source evaporation allowed studying a variety of compositions in the yttria-zirconia system and their influence on the CMAS/VA mitigation potential which is the topic of an upcoming paper.

4.3. Formation and progression of the reaction layer upon annealing

The common CMAS attack in EB-PVD 7YSZ coatings is characterized by the infiltration of the molten glass into the columnar gaps and porous features such as feather arms driven by capillary forces. Simultaneously, the molten glass generates dissolution of
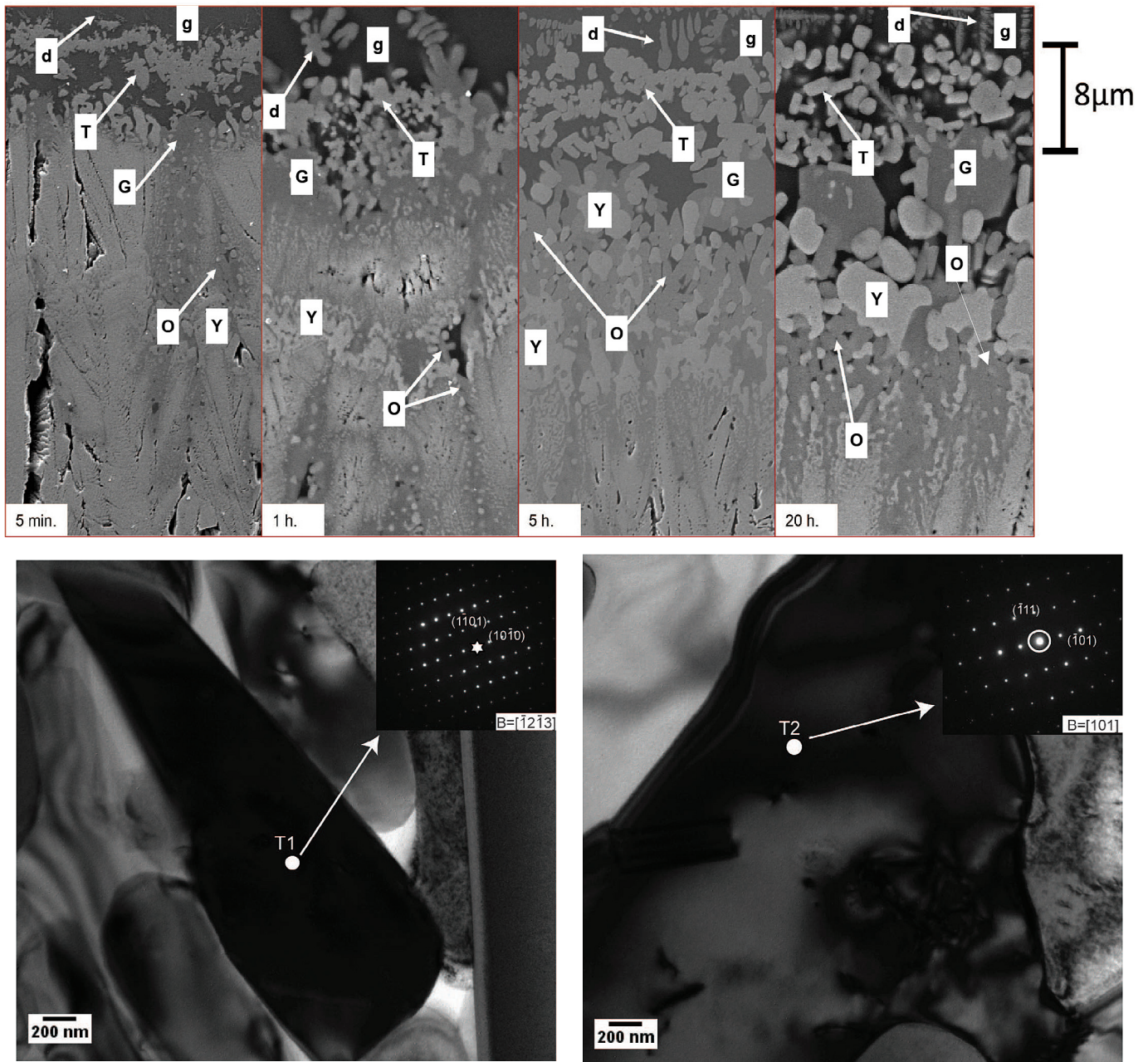
Fig. 10. (continued).

the t'-YSZ grains and re-precipitation as new Zr destabilized phases depending on the local chemistry of the glass [14]. Since 7YSZ does not generate a quick reaction with the molten glass due to the low yttria content, the molten glass does not have an agent to promote crystallization and remains in liquid phase, thus the gaps remain open for further infiltration. An optimal CMAS resistant coating needs to be designed in such a way that the crystallization of the glass happens fast enough to seal the gaps avoiding further infiltration. Additionally, after crystallization has taken place, the formed products should remain stable by having a minimal growth over time and not show further re-precipitation. Furthermore, studies have shown that the microstructure of the coating has an influence in reducing infiltration. This is achieved by adding more porous features to EB-PVD coatings which split the path that the molten glass has to travel, thus making the distribution of the melt more efficient throughout the coating by increasing its overall tortuosity [34]. In the case of yttria rich-zirconia coatings, upon glass infiltration, Y reacts quickly with the glass generating precipitation into stable phases that seal the columnar gaps and generate a uniform reaction layer that prevents further infiltration. Therefore, by combining a microstructure that distributes the flow more efficiently with a reactive material such as 65YZ a more effective infiltration resistance could be achieved. The summary of phases present at the reaction zone and at the inter-columnar gaps is shown in Fig. 12.

The reaction layer formed for CMAS 1 at the glass/TBC interface is mostly characterized by the uniform garnet (G) phase as seen in Fig. 13a Localized at the top of the coating and also at sealed columnar gaps which acts as the main CMAS arrest product. The top garnet phase exhibited a thickness increase with respect to time
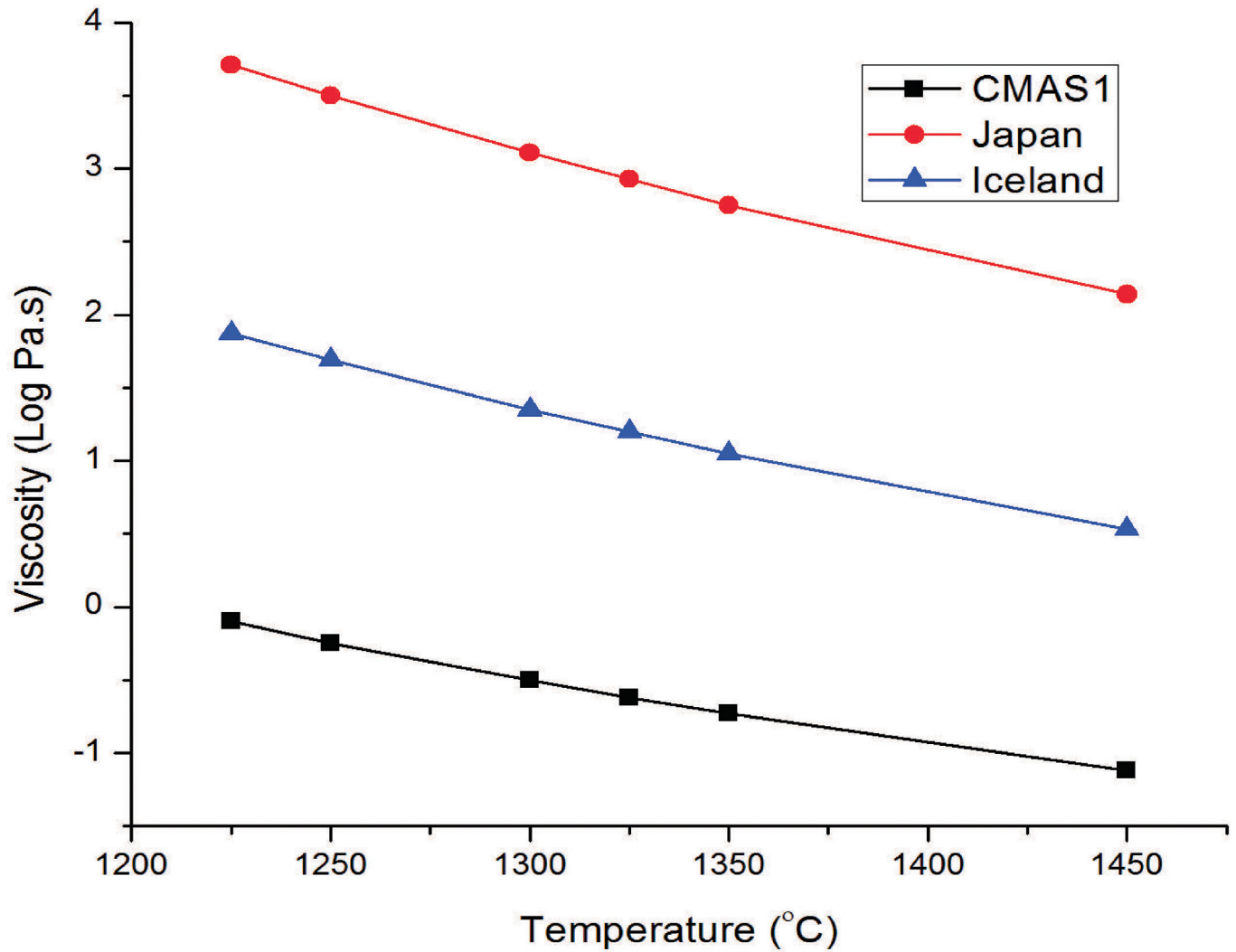
Fig. 11. Viscosity calculation plot for CMAS/VA compositions at different temperatures using the Giordano model [35].

Powder	Remarks	Phases at reaction zone		Phases at inter-columnar gaps	
		5 min	20 h	5 min	20 h
CMAS 1	Highest CaO	Garnet (G) $\longrightarrow$ Garnet		Garnet (G) $\longrightarrow$ Garnet	
		YSZ (Y) $\longrightarrow$ YSZ		Apatite (O) $\longrightarrow$ Apatite	
		Anorthite (A) $\longrightarrow$ Anorthite			
Japan VA	Highest SiO$_2$	Apatite (O) $\longrightarrow$ Apatite Yttrium - silicate (C)		Apatite $\longrightarrow$ Apatite	
		YSZ (Y) $\longrightarrow$ YSZ			
Iceland VA	Highest FeO	Garnet (G) $\longrightarrow$ Garnet		Garnet (G) $\longrightarrow$ Garnet	
		YSZ (Y) $\longrightarrow$ YSZ		Apatite (O) $\longrightarrow$ Apatite	
		Apatite (O) $\longrightarrow$ Apatite			
		YTFZ (T) $\longrightarrow$ YTFZ			
		Garnet dendrite $\longrightarrow$ Garnet dendrite (g)			

Fig. 12. Dominant phases formed within inter-columnar gaps and on top of the coating in the reaction layer during CMAS/VA crystallization for the used CMAS/VA compositions tested at 1250 °C.
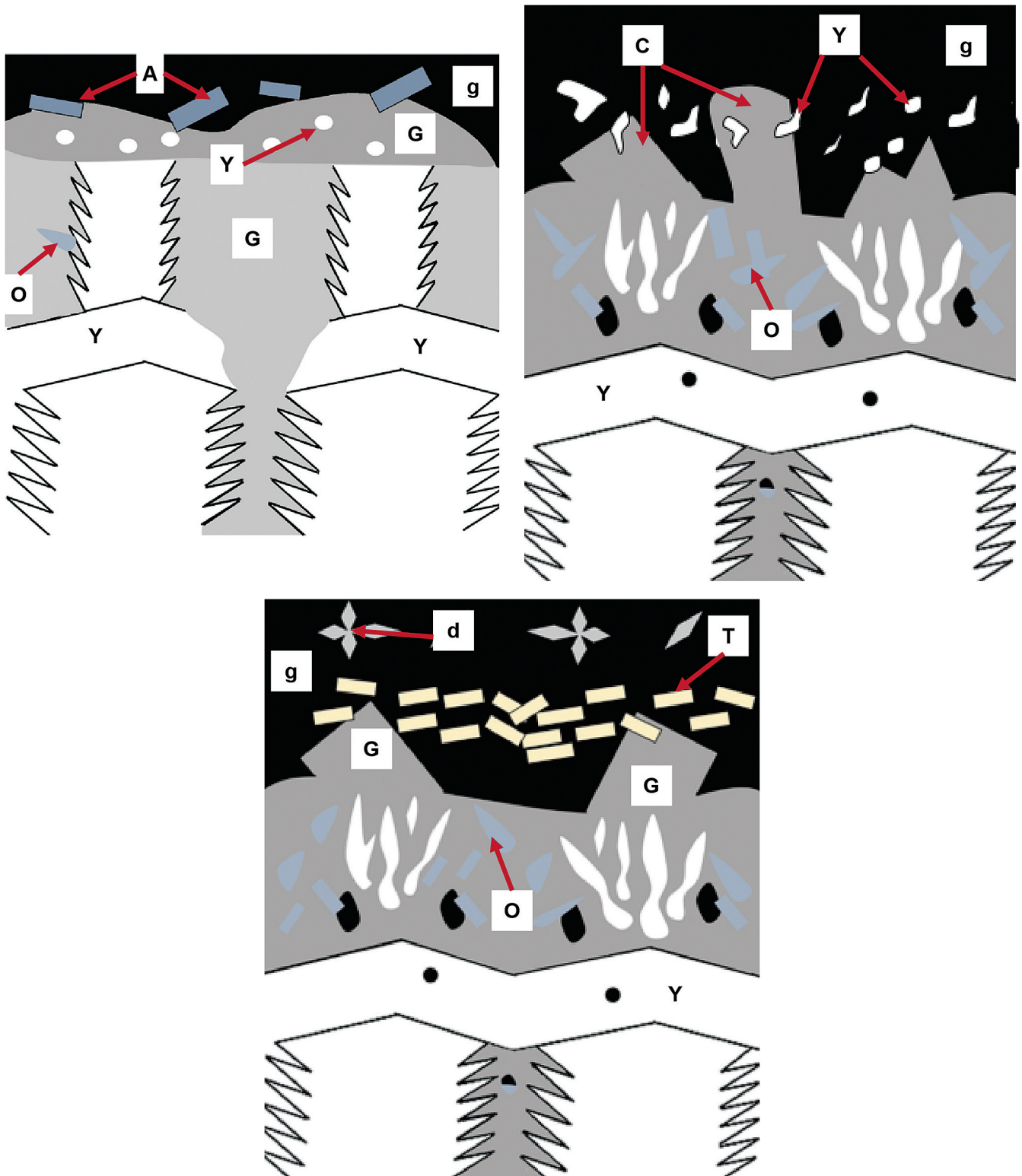
Fig. 13. a: Reaction layer schematic for CMAS 1 at 1250 °C. b: Reaction layer schematic for Japan VA at 1250 °C. c: Reaction layer schematic for Iceland VA at 1250 °C.

starting from 4 μm after 5 min to 21 μm after 20 h. The general garnet structure is represented by the following formula: $X_3Y_2Z_3O_{12}$ [10,28], where X is formed by Ca^{+2}, Mg^{+2}. Y represents Zr^{+2}, Y^{+3}, Ti^{+4}, Fe^{+2}. Finally, Z is formed by Al^{+3}, Fe^{+3}, Si^{+4} [10]. The calculated garnet formula using Table 2a composition for 20 h garnet is $(Ca_{1.59}, Mg_{0.89})_3(Y_{1.42}, Ti_{0.52})_2(Al_{1.27}, Fe_{0.65}, Si_{2.29})_3O_{12}$. CMAS

1 and Iceland VA show a higher content in Fe and Ti compared to Japan VA. It appears that the mentioned elements promote the formation of garnet products since Japan VA does not exhibit garnet formation. The high presence of Ca in CMAS 1 appears to be enough to form garnet and anorthite in the reaction zone. The anorthite phase is a stable product which has been reported to generate

CMAS arresting properties in mitigation strategies using Al_2O_3+TiO_2 doping in 7YSZ coatings [20,23,37]. However, the anorthite phase present in this study was always found lying on top of the garnet acting more as a sub-reaction product with no columnar gap sealing properties. Subsequently, the formation of the anorthite phase (A) induces the continuous reaction of Fe with Y and CMAS elements promoting the constant growth of the garnet phase (G) which represents the dominating phase formed upon reaction of CMAS 1 and yttria. The YSZ layer (Y) is formed as a sub-product from the transport of Y from the TBC into the glass which is used to initialize the crystallization of the glass forming reaction products. The diffusion of Y into the glass generates a reduction in Y content in the TBC which promotes the formation of Y-Zr (Y) particles with a higher Zr content than the original exhibited in the coating. The YSZ layer exhibits a growth with time from 3 μm after 5 min to 5.8 μm after 20 h which confirms the constant depletion of Y reacting with the glass promoting the stabilization of the YSZ-Zr rich phase. Table 2a shows the composition of the reaction products for 5 min and 20 h of heat treatment for CMAS 1. The chemical composition of the products does not show a significant variation over time suggesting the stability of the formed reaction products. The YSZ layer exhibits a reduction in Y after 20 h as expected due to the constant Y diffusion which promotes the formation of the garnet phase.

Fig. 13b shows the schematic representation of the reaction layer formation for Japan VA. The reaction layer exhibits a different configuration compared to CMAS 1 where the reaction product concentrates uniformly on top of the coating. For the Japan VA case, the apatite and yttrium silicate phases (O and C respectively) were found in coexistence with the degraded TBC columns during all the long term tests (1−20 h). Due to the low Fe content in the Japan VA, no significant traces of garnet are found making the main reaction product apatite. Due to this fact, the garnet phase is neglected as effective reaction product for Japan VA. The highly Si rich Japan ash initializes the reaction by diffusing Y from the coating forming initially (5 min) small Ca-Si-Y apatite crystals (O) in columnar gaps with a higher Ca content as seen in Table 2c. As time progresses, the constant reaction of the Si rich glass and Y generates the formation of the yttrium silicate phase (C) (Fig. 9b) which grows progressively with time as large faceted yttrium silicate (C) particles after 20 h as seen in Fig. 10b. This process is characterized by a slow diffusion rate from the interaction of the high Si unreacted glass (g) with the coating. The apatite crystals are still traced after 20 h appearing as small prismatic particles with a chemical composition matching the one for the particles formed after 5 min. From the chemical composition in Table 2b the composition for the "O" particles after 20 h fall close with the range of the $Ca_2Y_8(SiO_4)O_2$ (Ca = 12.5%, Si = 37.5%, Y = 50%) phase found in the XRD studies. Additionally, the hexagonal apatite phase was confirmed by TEM results in Fig. 10d obtained from 20 h infiltrated sample. On the other hand, the "C" particles exhibited a higher Si content compared with the "O" phase. TEM results shown in Fig. 10e from the 20 h infiltrated sample confirmed the phase to be monoclinic $Y_2Si_2O_7$. The dominating phase forming upon glass crystallization for Japan VA appears to be the apatite which is traced in all tests performed (from 5 min to 20 h). The large faceted yttrium silicate (C) appears to be a reaction product that only forms at the glass/TBC interface and it is only traced after long term (from 1 to 20 h) of infiltration tests. Lastly, the chemical composition of the "C" products (high Si, low Ca and Zr) and the peak overlap for the $Y_{9.33}(SiO_4)_6O_2$ phase found in XRD studies could lead to a misinterpretation of the phase as a form of Ca-lean apatite. The YSZ phase (Y) exhibits the same trend exhibited for CMAS 1 with a characteristic accumulation of Zr due to the Y diffusion into the glass.

The reaction layer generated for the Iceland VA exhibits a similar configuration as the one exhibited by Japan VA as seen in Fig. 13c. The configuration is also characterized by the initial mixture of reaction products with degraded TBC columns. In this case the initial reaction is initialized by the formation of the small prismatic apatite (O) products containing Ca-Si-Y. Apatite crystals were found embedded in large garnet (G) particles which makes apatite the dominant phase blocking CMAS glass for infiltration in early stages (5 min). The Fe-Y rich garnets (G) containing Ca-Mg-Al-Si are identified after 1 h of infiltration testing. It is clear from the results that the key element promoting the garnet phase formation is Fe. The calculated formula for Iceland VA garnet from Table 2c for 20 h is $(Ca_{0.85},Mg_{0.90})_3(Y_{2.45},Ti_{0.37})_2(Al_{0.99},Fe_{1.12},Si_{1.89})_3O_{12}$. Furthermore, due to the large glass reservoir deposited, the time progression (over 5 h) generates a continuous diffusion of Y into the glass inducing the formation of the top glass embedded garnet/dendritic particles (d). It is still under investigation if the dendrites are formed during cooling of the saturated Y glass. More detailed high temperature XRD analysis and thermal tests at different cooling rates will be performed to have an insight on the precipitation of the dendritic particles. Additionally, it appears that the constant Y diffusion from the reaction zone which induces the formation of dendrites generates a depletion of the garnet phase formed at the reaction interface. The recession in the garnet phase is noted after 5 h of heat treatment (Fig. 10c). The depletion of the uniform conglomerated garnet layer (G) generated after 1 h is exhibited by reducing from 20 μm thickness to localized garnet particles after 20 h with thicknesses of 10 μm max. The depletion in Fe at the reaction layer interface due to the constant formation of garnet-dendrites facilitates the formation of apatite prismatic particles which take over the reaction as main crystallization products after 20 h of heat treatment. The mechanism controlling the glass crystallization for Iceland VA appears to be due to the combination of the apatite and garnet phases coexisting throughout the performed infiltration tests.

The available Ti and Fe in the Iceland VA composition generates the formation of the YTFZ (T) sub-reaction product accumulated on top of the reaction layer. The chemical composition shown in Table 2c clearly exhibits a similar amount of Fe and Ti in the phase. From the XRD results, the YTZ (T) and YSZ (Y) phases exhibited a peak overlap for Iceland VA. It appears that Fe and Ti have a tendency to form a Zr stabilized product since the YSZ (Y) phase shows an increase in Fe and Ti after 20 h as seen in Table 2. This could mean that the T product represents a Ti-Fe-Y stabilized zirconia phase (YTFZ). The latter particles are not believed to have significance in the crystallization of the glass at the reaction layer. However, due to their Y enrichment, they could be serving as Y source for the formation of the top garnet/dendritic particles. The YSZ (Y) layer at the bottom of the reaction zone exhibits similar composition and appearance for all the CMAS/VA compositions. Table 2c shows the chemical composition summary of the reaction products for Iceland VA. It exhibits an increase in the Y content and depletion of Zr for the garnetdendrite particles after 20 h. This could confirm that their formation in interaction with the glass reservoir acts as a sink for Y which reduces the garnet presence at the reaction layer and increases the formation of apatite crystals. Finally, it is difficult to properly characterize the formed phases by only using EDS/XRD analysis. A TEM analysis will be carried out in the future with coatings with same composition and improved microstructural features.

5. Conclusions

Yttria rich zirconia thermal barrier coatings with an overall composition of 65 wt % yttria (65YZ) were successfully deposited by EB-PVD, using two-source evaporation and jumping beam

technology. The coatings were infiltrated by one CMAS and two volcanic ashes (VA) at 1250 °C for a time range varied from 5 min to 20 h. The infiltration resistance of the coatings and formed reaction products were studied by means of SEM on infiltrated samples and XRD studies on yttria rich-zirconia and CMAS/VA powder mixtures. The main outcome of this work is as follows:

- The 65YZ coatings exhibited promising results for CMAS/VA infiltration resistance due to the formation of apatite and garnet phases which have excellent potential for CMAS mitigation. The rapid crystallization of these phases considerably lowered the infiltration depth of the deposits and left the main coating unaffected.
- The new phases are formed by the reaction of Yttrium from the coating -with the molten glass, thereby generating its rapid crystallization (rapid phase formation already after 5 min of annealing). Additionally, the reaction products appear to be stable after long term heat treatment by maintaining the columnar gaps sealed and generating a uniform reaction layer on top of the TBC with a minimum growth over time.
- The presence of Fe in the glass for CMAS 1 and Iceland VA promotes the formation of a new Fe-Y rich garnet phase which has not been previously reported in literature.
- The infiltration results have shown a different morphology and chemistry of the reaction products depending on the local chemistry of the molten glass. Calculated viscosity data could explain the observed differences in infiltration depth at the early infiltration testing with the highest infiltration depth for the deposit with the lowest viscosity.
- The reaction products exhibited a slight variation in their chemical composition. In case of Japan VA, the yttrium silicate phase was found after long term infiltration (1−20 h) which has not been previously reported in literature. Iceland VA exhibited a reduction in the garnet phase after 5 h due to a constant Y diffusion mechanism. The described mechanism appears to constantly diffuse Y from the reaction zone into the molten glass reservoir promoting the formation of the dendritic garnets (d) and reducing the uniform garnet (G) layer formed until 5 h of infiltration testing.
- The effects of coating microstructure on infiltration resistance are clearly seen in this study by deeper infiltration into wider inter-columnar gaps. It is believed that an improvement in the infiltration resistance can be reached by generating a coating with smaller columnar gaps with less openings for infiltration thus, reducing the deep localized infiltrated zones.
- An assessment on the spallation behavior of the reaction layer, the erosion behavior of YZ, and compatibility with a base 7YSZ layer has to be tested in future. The optimal Y-Zr ratio for infiltration mitigation will be determined as well.

References

[1] N.P. Padture, M. Gell, E.H. Jordan, Thermal barrier coatings for gas-turbine engine applications, Science 296 (5566) (2002) 280–284, http://dx.doi.org/10.1126/science.1068609.

[2] R. Darolia, Thermal barrier coatings technology: critical review, progress update, remaining challenges and prospects, Int. Mater. Rev. 58 (6) (2013) 315–348.

[3] U. Schulz, et al., Review on advanced EB-PVD ceramic topcoats for TBC applications, Int. J. Appl. Ceram. Technol. 1 (4) (2004) 302–315.

[4] D.R. Clarke, M. Oechsner, N.P. Padture, Thermal-barrier coatings for more efficient gas-turbine engines, MRS Bull. 37 (10) (2012) 891–898.

[5] J.P. Bons, et al., High-pressure turbine deposition in land-based gas turbines from various synfuels, J. Eng. Gas Turbines Power 129 (1) (2007) 135–143.

[6] J. Webb, et al., Coal ash deposition on nozzle guide Vanes—Part I: experimental characteristics of four coal ash types, J. Turbomach. 135 (2) (2013) 021033.

[7] C.G. Levi, et al., Environmental degradation of thermal-barrier coatings by molten deposits, MRS Bull. 37 (10) (2012) 932–941.

[8] K. Lee, et al., Mechanisms and mitigation of volcanic ash attack on yttria stablized zirconia thermal barrier coatings, Surf. Coatings Technol. 260 (2014) 68–72.

[9] R. Naraparaju, et al., The accelerating effect of CaSO4 within CMAS (CaO−MgO−Al2O3−SiO2) and its effect on the infiltration behavior in EB-PVD 7YSZ, J. Am. Ceram. Soc. 99 (4) (2016) 1398–1403.

[10] W. Braue, P. Mechnich, Recession of an EB-PVDYSZ coated turbine blade by CaSO4 and fe, Ti-Rich CMAS-Type deposits, J. Am. Ceram. Soc. 94 (12) (2011) 4483–4489.

[11] P. Mechnich, W. Braue, U. Schulz, High-Temperature corrosion of EB-PVD yttria partially stabilized zirconia thermal barrier coatings with an artificial volcanic ash overlay, J. Am. Ceram. Soc. 94 (3) (2011) 925–931.

[12] C. Mercer, et al., A delamination mechanism for thermal barrier coatings subject to calcium−magnesium−alumino-silicate (CMAS) infiltration, Acta Mater. 53 (4) (2005) 1029–1039.

[13] M.P. Borom, C.A. Johnson, L.A. Peluso, Role of environment deposits and operating surface temperature in spallation of air plasma sprayed thermal barrier coatings, Surf. Coatings Technol. 86 (1996) 116–126.

[14] S. Krämer, et al., Thermochemical interaction of thermal barrier coatings with molten CaO−MgO−Al2O3−SiO2 (CMAS) deposits, J. Am. Ceram. Soc. 89 (10) (2006) 3167–3175.

[15] E.M. Zaleski, C. Ensslen, C.G. Levi, Melting and crystallization of silicate systems relevant to thermal barrier coating damage, J. Am. Ceram. Soc. 98 (5) (2015) 1642–1649.

[16] G. Pujol, et al., Step-by-step investigation of degradation mechanisms induced by CMAS attack on YSZ materials for TBC applications, Surf. Coatings Technol. 237 (2013) 71–78.

[17] U. Kueppers, et al., The thermal stability of eyjafjallajökull ash versus turbine ingestion test sands, J. Appl. Volcanol. 3 (1) (2014) 1.

[18] R.J. Clarkson, E.J. Majewicz, P. Mack, A re-evaluation of the 2010 quantitative understanding of the effects volcanic ash has on gas turbine engines, Proc. Inst. Mech. Eng. Part G J. Aerosp. Eng. (2016), 0954410015623372.

[19] J.M. Drexler, A.L. Ortiz, N.P. Padture, Composition effects of thermal barrier coating ceramics on their interaction with molten Ca−Mg−Al−silicate (CMAS) glass, Acta Mater. 60 (15) (2012) 5437–5447.

[20] A. Aygun, et al., Novel thermal barrier coatings that are resistant to high-temperature attack by glassy deposits, Acta Mater. 55 (20) (2007) 6734–6745.

[21] P. Mechnich, W. Braue, Volcanic Ash-Induced decomposition of EB-PVD Gd2Zr2O7 thermal barrier coatings to Gd-Oxyapatite, zircon, and gd, Fe-Zir-conlite, J. Am. Ceram. Soc. 96 (6) (2013) 1958–1965.

[22] S. Krämer, J. Yang, C.G. Levi, Infiltration-Inhibiting reaction of gadolinium zirconate thermal barrier coatings with CMAS melts, J. Am. Ceram. Soc. 91 (2) (2008) 576–583.

[23] J.M. Drexler, et al., Jet engine coatings for resisting volcanic ash damage, Adv. Mater. 23 (21) (2011) 2419–2424.

[24] A.R. Krause, et al., 2ZrO2· Y2O3 thermal barrier coatings resistant to degradation by molten CMAS: Part I, optical basicity considerations and processing, J. Am. Ceram. Soc. 97 (12) (2014) 3943–3949.

[25] A.R. Krause, et al., 2ZrO2· Y2O3 thermal barrier coatings resistant to degradation by molten CMAS: Part II, interactions with sand and fly ash, J. Am. Ceram. Soc. 97 (12) (2014) 3950–3957.

[26] A.K. Rai, et al., CMAS-resistant thermal barrier coatings (TBC), Int. J. Appl. Ceram. Technol. 7 (5) (2010) 662–674.

[27] R. Darolia, et al., Layered Thermal Barrier Coatings Containing Lanthanide Series Oxides for Improved Resistance to CMAS Degradation, 2006.

[28] N.K. Eils, P. Mechnich, W. Braue, Effect of CMAS deposits on MOCVD coatings in the system Y2O3−ZrO2: phase relationships, J. Am. Ceram. Soc. 96 (10) (2013) 3333–3340.

[29] A.R. Krause, X. Li, N.P. Padture, Interaction between ceramic powder and molten calcia-magnesia-alumino-silicate (CMAS) glass, and its implication on CMAS-resistant thermal barrier coatings, Scr. Mater. 112 (2016) 118–122.

[30] W. Li, et al., Air plasma-sprayed yttria and yttria-stabilized zirconia thermal barrier coatings subjected to calcium-magnesium-alumino-silicate (CMAS), J. Therm. Spray. Technol. 23 (6) (2014) 975–983.

[31] R. Naraparaju, et al., Degradation study of 7wt.% yttria stabilised zirconia (7YSZ) thermal barrier coatings on aero-engine combustion chamber parts due to infiltration by different CaO−MgO−Al 2 O 3−SiO 2 variants, Surf. Coatings Technol. 260 (2014) 73–81.

[32] O. Fabrichnaya, F. Aldinger, Assessment of thermodynamic parameters in the system ZrO2−Y2O3−Al2O3, Z. Für Met. 95 (1) (2004) 27–39.

[33] V.G. Varanasi, T.M. Besmann, T.J. Anderson, Equilibrium analysis of CVD of

yttria-stabilized zirconia, J. Electrochem. Soc. 152 (1) (2005) C7–C14.

[34] R. Naraparaju, et al., Tailoring the EB-PVD columnar microstructure to mitigate the infiltration of CMAS in 7YSZ thermal barrier coatings, J. Eur. Ceram. Soc. 37 (2017) 261–270, http://dx.doi.org/10.1016/j.jeurceramsoc.2016.07.027.

[35] D. Giordano, J.K. Russell, D.B. Dingwell, Viscosity of magmatic liquids: a model, Earth Planet. Sci. Lett. 271 (1) (2008) 123–134.

[36] U. Schulz, J. Miinzer and U. Kaden. MICROSTRUCTURE OF EB-PVD TBCs. Presented at 26th Annual Conference on Composites, Advanced Ceramics, Materials, and Structures-B: Ceramic Engineering and Science Proceedings, Volume 23. 2009.

[37] J.M. Drexler, et al., Air-plasma-sprayed thermal barrier coatings that are resistant to high-temperature attack by glassy deposits, Acta Mater. 58 (20) (2010) 6835–6844.